Title

Discharge Characteristics of Lithium Battery Electrodes with a Semiconducting Polymer Studied by Continuum Modeling and Experiment

Journal

Journal of The Electrochemical Society, 161(12)

ISSN

0013-4651

Authors

Wu, Shao-Ling
Javier, Anna E
Devaux, Didier
et al.

Publication Date

2014

DOI

10.1149/2.0261412jes

Peer reviewed

Discharge Characteristics of Lithium Battery Electrodes with a Semiconducting Polymer Studied by Continuum Modeling and Experiment

Shao-Ling Wu,[a,b] Anna E. Javier,[a,b,*] Didier Devaux,[a,c] Nitash P. Balsara,[a,b,c,d,*] and Venkat Srinivasan[a,b,*,z]

[a]*Environmental Energy Technologies Division, Lawrence Berkeley National Laboratory, Berkeley, California 94720, USA*
[b]*Joint Center for Energy Storage Research (JCESR), Lawrence Berkeley National Laboratory, Berkeley, California 94720, USA*
[c]*Materials Sciences Division, Lawrence Berkeley National Laboratory, Berkeley, California 94720, USA*
[d]*Department of Chemical and Biomolecular Engineering, University of California, Berkeley, California 94720, USA*

Conducting polymers such as poly(3-hexylthiophene) (P3HT) can be used to convey electronic charge in battery electrodes. The electronic conductivity of P3HT (and other electronically conducting polymers) is potential-dependent. The main advance in this work is to quantify the effect of this potential dependency on battery performance. The discharge characteristics of a battery consisting of a cathode with $LiFePO_4$ particles in a poly(3-hexylthiophene)-*b*-poly(ethylene oxide) (P3HT-PEO) copolymer matrix that conveys electrons and ions to the active particles, a polystyrene-*b*-poly(ethylene oxide) (PS-PEO) copolymer electrolyte layer, and a lithium metal anode were examined by experiments and macro-homogeneous modeling; lithium bis (trifluoromethanesulfonyl) imide was the salt in the cathode and the electrolyte. By comparing the model predictions with experiments, we conclude that the electronic conductivity of the polymer in the cathode is significantly lower than that obtained from measurements in the absence of active particles. The potential-dependent conductivity is manifested in the shape of the discharge curve wherein the slope increases continuously with capacity. The model provides insight into the underpinnings of the observed rate-dependency of electrode capacity, thereby guiding the design of the next generation of electrodes.
 [DOI: 10.1149/2.0261412jes]

Manuscript submitted June 13, 2014; revised manuscript received July 21, 2014. Published August 27, 2014.

In conventional rechargeable lithium-ion batteries, a slurry of active particles such as $LiFePO_4$, graphite, or $LiCoO_2$ are mixed with electronically conducting carbon particles and an inert polymer binder such as poly(vinylidene fluoride) (PVDF) and cast onto a current collector to yield porous electrodes. In the last step of battery assembly, the pores in the electrode are filled with a liquid electrolyte. During discharge of the cathode, electrons flow to the active particles through the conducting carbon network while the electrolyte in the pores conveys the lithium ions necessary to complete the redox reaction. An example of such a reaction is

$$Li^+ + 1e^- + FePO_4 \leftrightarrow LiFePO_4 \quad [1]$$

The reverse reaction above occurs during charge. The resistance to electron transport is independent of time and electrode potential in conventional batteries as the carbon particles form a simple ohmic conducting network.

There have been many previous studies wherein electronic charge in a battery electrode is conveyed by a conducting polymer such as poly(3-hexylthiophene) (P3HT).[1] The main difference between such electrodes and conventional battery electrodes is that the polymer is a semiconductor wherein electronic conductivity is a function of electrode potential. In addition to oxidation and reduction of the active particles (Reaction 1), the conducting polymer gets oxidized and reduced. An example of such a reaction is

$$P3HT \leftrightarrow P3HT^+ + 1e^- \quad [2]$$

where $P3HT^+$ represents a P3HT chain with one oxidized monomer. We note in passing that P3HT is a hole conductor and the formal reaction should have h^+ on the left hand side of Reaction 2 instead of $1e^-$ on the right hand side. In electrodes with a conducting polymer Reactions 1 and 2 occur simultaneously during charge and discharge. The electronic conductivity of P3HT is a strong function of the fraction of oxidized monomers ($P3HT^+$) which in turn depends on electrode potential. The introduction of semiconducting polymers in battery electrodes thus enables control strategies that are not possible in conventional electrodes. For example, one could design a cathode wherein the charging rate is higher than the discharging rate by exploiting the difference in potential during charge and discharge. Additionally, the electronically conducting polymer has the potential to improve cell energy density and power if it can be used as a replacement for chemically inactive binders such as PVDF.

The purpose of this paper is to develop a continuum model that accounts for the presence of a semiconducting polymer in a battery electrode. We compare the predictions of this model with experiments conducted on an all-solid-state cell with $LiFePO_4$ cathode and a lithium metal anode. The cathode comprised a poly(3-hexylthiophene)-*b*-poly(ethylene oxide) (P3HT-PEO) copolymer, lithium bis (trifluoromethanesulfonyl) imide (LiTFSI), and $LiFePO_4$ particles. The P3HT-PEO/LiTFSI mixture is microphase separated with the P3HT domains providing electron transport and the PEO/LiTFSI domains providing ion transport to the active particles.[2–4] The P3HT-PEO/LiTFSI mixture thus performs all of the supporting functions in the cathode including binding the active particles and providing avenues for charge transport. The separator comprised a poly(styrene)-*b*-poly(ethylene oxide) (PS-PEO) copolymer and LiTFSI.[5,6]

Simulations show that the decreasing electronic conductivity during discharge is an essential feature that governs the shape of the potential vs. capacity curve. The model is used to provide insight into the nature of the discharge process: state-of-charge (SOC) of the electrode and electronic conductivity of the P3HT-PEO binder as a function of distance from the current collector. The model also enables determining the factors that limit the performance of this all-solid-state cell.

Experimental

The synthesis of the P3HT-PEO binder and the PS-PEO electrolyte are reported in previous publications.[2,6] The molecular weights of the P3HT and PEO blocks were 6 and 2 kg/mol. The molecular weights of the PS and PEO blocks were 240 and 269 kg/mol. The $LiFePO_4$ (P2

*Electrochemical Society Active Member.
zE-mail: vsrinivasan@lbl.gov

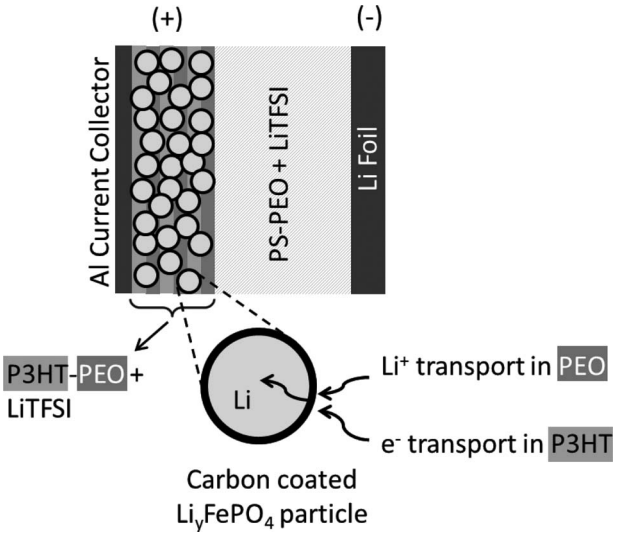

Figure 1. Schematic of cell used in this study. The positive electrode consists of carbon-coated $LiFePO_4$ dispersed in P3HT-PEO block copolymer. The electrode is casted on an aluminum current collector. The negative electrode is lithium foil which also serves as the reference electrode. Separating the positive and negative electrode is a PS-PEO block copolymer layer that serves as a separator and the medium for ionic conduction. LiTFSI salt is added to both P3HT-PEO and PS-PEO copolymer with a concentration of $r_0 = 0.085$, where r_0 is the molar ratio of lithium ions to ethylene oxide moieties. The transport of a lithium ion and an electron during discharge is depicted.

grade) active material was obtained from Phostech Lithium, and dried overnight at 120°C prior to use. The cathode solution was prepared by dissolving P3HT-PEO (0.0944 g) and LiTFSI (0.0126 g) in anhydrous tetrahydrofuran (THF) (3 mL). $LiFePO_4$ (0.2515 g) was then added to the solution and mixed thoroughly using a homogenizer for ca. 5 minutes. This solution was then cast on electrical grade aluminum current collector foil, spread evenly using a doctor blade, and dried under vacuum at 70°C overnight. A cathode film (5 μm thick) was punched out of the dry film and hand-pressed on a 1 cm^2 PS-PEO polymer electrolyte film (40-50 μm thick). A lithium metal anode (150 μm thick) was pressed to the other side of the PS-PEO polymer electrolyte (or separator). These were then assembled in pouch cells with a nickel tab on the negative electrode and an aluminum tab on the positive electrode. The entire assembly was sealed in an aluminum-laminated pouch material (Showa Denko) using a vacuum sealer (Packaging Aids Corp) for an air-free atmosphere.

Battery cycling was performed with a Maccor ovens and instruments at 90°C. Constant current (10 μA/cm^2) was used to charge the battery to 3.6 V and then followed by a 1 h rest period. This was followed by a constant current discharge step to 3.1 V at the c-rate of interest followed by another 1 h rest period. This was then followed by a slow constant current (10 μA/cm^2) discharge to fully discharge the battery before starting the next experiment. The slow discharge step was also used to confirm that the battery capacity had not faded.

Model Development

Figure 1 shows the schematic of the battery consisting of a $LiFePO_4$ positive electrode and a Li foil negative electrode. The carbon coated $LiFePO_4$ particles are dispersed in the P3HT-PEO/LiTFSI mixture. For simplicity, the P3HT-PEO block copolymer is illustrated as vertically aligned lamellar domains that provide pathways for electron and ion transport. In reality, the block copolymer is composed of a large number of randomly oriented lamellae. Between the positive and negative electrodes is the PS-PEO/LiTFSI block copolymer electrolyte layer. When passing current, lithium ions travel through the PEO domains of the PS-PEO and P3HT-PEO block copolymers, while electrons travel through the external circuit and the P3HT domains of the P3HT-PEO block copolymer. During discharge, lithium ions and electrons react at the surface of the active material. The mathematical model used in this study is based on the macro-homogeneous model developed by Newman and coworkers.[7,8] Table I summarizes the model equations used in this study. The ionic transport in the block copolymer binder and electrolyte is similar to that in the solution phase of a porous electrode. Concentrated solution theory is used to describe mass transport of the salt in the electrolyte and the electrode (equation 3). A modified Ohm's law that includes the concentration overpotential is used to calculate the potential in the ionically-conductive phase of the block copolymer (equation 4). The potential drop in the active material is calculated by taking into account the dependency of electronic conductivity of the binder on the potential (equation 5). The change in ionic current is equated to the rate of charge transfer (equation 6). Butler-Volmer kinetics is used to account for the charge-transfer reaction (equations 7 and 8). The mass balance of lithium in the active material, neglecting migration effects, is governed by Fick's diffusion equation (equation 9). Details for the mathematical developments of the porous electrode model are given in the literature.[8–10] Similar equations (equations 10–13) are used to model a lithium-PS-PEO-lithium symmetric cell.

Several assumptions are made in the model of this study. The composite cathode is composed of two phases, $LiFePO_4$ particles and P3HT-PEO block copolymer binder; the electrolyte layer is composed of only one phase, PS-PEO block copolymer. No pores are present in the entire battery. Contact resistances between the current collector and the electrode and that between the $LiFePO_4$ particles and the electronically conductive binder are assumed to be negligible.

It is known that $LiFePO_4$ electrode undergoes a phase change during lithium intercalation and deintercalation.[11–13] The classic shrinking-core model [14] was found to be invalid since lithium diffusion is anisotropic [15] and both lithiated and delithiated phases were found on the surface of the particles.[16] Other mechanisms [15–18] have been proposed to describe the phase transition process but they remain controversial. For simplicity, our model does not consider the phase change of $LiFePO_4$ particles. We show below that the electronic conductivity of the binder is the factor that governs the performance of the device, and thus our use of a simplified model to describe transport within $LiFePO_4$ particles is justified.

Figure 2a shows the electronic conductivity (σ) of P3HT-PEO(6-2) block copolymer as a function of cell potential at 90°C. The experimental data (open circles) is taken from impedance measurements using a three-electrode electrochemical cell reported in the previous study.[4] The logarithm of electronic conductivity is linearly dependent on electrode potential, and the linear fit (solid line, σ) is used in the model calculations. Figure 2a also shows a dashed line, which is the fitted conductivity divided by 40 (σ/40), and three constant values; these values are used in later calculations. Figure 2b shows the ionic conductivity (κ) of PS-PEO(240-269) block copolymer as a function of electrolyte concentration, measured at 90°C by ac impedance spectroscopy using stainless steel symmetrical cells.[6] The ionic conductivity of P3HT-PEO is assumed to be the same as that of PS-PEO block copolymer. The diffusion coefficient (D_i) of LiTFSI in PS-PEO has only been measured at one concentration [19]; we use this value for both P3HT-PEO and PS-PEO regardless of salt concentration.

Similar to a porous electrode in which mass and charge transport is obstructed by tortuous paths, the conductivities and diffusion coefficients are reduced in the conducting copolymer binder due to the presence of the active material particles. The effective conductivities and diffusion coefficient can be estimated from bulk values, the volume fraction of the transporting phase (ε), and the tortuosity (τ) within the electrode,

$$\sigma_{\text{eff}} = \sigma\frac{\varepsilon}{\tau} \text{ or } \kappa_{\text{eff}} = \kappa\frac{\varepsilon}{\tau} \text{ or } D_{i,\text{eff}} = D_i\frac{\varepsilon}{\tau} \qquad [14]$$

where the subscript, eff, stands for the effective quantity of the corresponding parameter. Since the P3HT-PEO copolymer conducts both electrons and ions, the same conducting phase volume fraction, ε, is

Table I. Summary of model equations used for Li/LiFePO$_4$ cell and Li/Li symmetric cell.

	Governing equations		Boundary conditions
Li/LiFePO$_4$ cell			
Mass balance (ionic phase)	$\frac{\partial \varepsilon c_2}{\partial t} = \nabla \cdot \left(D_{i,\text{eff}} \nabla c_2\right) + \frac{a\left(1-t_+^0\right)}{F} i_n$	[3]	$\left.\frac{\partial c_2}{\partial x}\right\|_{x=0} = 0, -D_{i,\text{eff}} \left.\frac{\partial c_2}{\partial x}\right\|_{x=L_{\text{pos}}+L_{\text{sep}}} = \frac{1-t_+^0}{F} I_{\text{app}}$
Modified Ohm's law (ionic phase)	$\mathbf{i}_2 = -\kappa_{\text{eff}} \nabla \Phi_2 + \frac{2\kappa_{\text{eff}} RT}{F}\left(1+\frac{\partial \ln f_\pm}{\partial \ln c_2}\right)\left(1-t_+^0\right)\nabla \ln c_2$	[4]	$\left.\frac{\partial \Phi_2}{\partial x}\right\|_{x=0} = 0, \left. i_2\right\|_{x=L_{\text{pos}}+L_{\text{sep}}} = i_{0,\text{Li}}$
Ohm's law (electronic phase)	$\nabla \cdot \mathbf{i}_1 = \nabla \cdot (-\sigma_{\text{eff}} \nabla \Phi_1)$	[5]	$\left[\exp\left(-\frac{\alpha_a F}{RT}\Phi_2\right) - \exp\left(\frac{\alpha_c F}{RT}\Phi_2\right)\right], i_{0,\text{Li}} = F k_{\text{Li}} c_2^{\alpha_a}$ $i_1\|_{x=0} = I_{\text{app}}, i_1\|_{x=L_{\text{pos}}} = 0$
Current balance	$\nabla \cdot \mathbf{i}_1 = -\nabla \cdot \mathbf{i}_2 = -a i_n$	[6]	
Reaction rate (Butler-Volmer equation)	$i_n = i_0\left[\exp\left(\frac{\alpha_a F}{RT}\left(\Phi_1 - \Phi_2 - U_{\text{eq}}\right)\right) - \exp\left(-\frac{\alpha_c F}{RT}\left(\Phi_1 - \Phi_2 - U_{\text{eq}}\right)\right)\right]$	[7]	
	$i_0 = F k c_2^{\alpha_a} (c_{1,\max} - c_1\|_{r=r_p})^{\alpha_a} (c_1\|_{r=r_p})^{\alpha_c}$	[8]	
Mass balance (active particle)	$\frac{\partial c_1}{\partial t} = \nabla \cdot (D_{\text{Li}} \nabla c_1)$	[9]	$\left.\frac{\partial c_1}{\partial r}\right\|_{r=0} = 0, -D_{\text{Li}} \left.\frac{\partial c_1}{\partial r}\right\|_{r=r_p} = \frac{i_n}{F}$
Li/Li symmetric cell			
Mass balance (ionic phase)	$\frac{\partial c_2}{\partial t} = \nabla \cdot \left(D_{i,\text{eff}} \nabla c_2\right)$	[10]	$-D_{i,\text{eff}} \left.\frac{\partial c_2}{\partial x}\right\|_{x=0} = \frac{1-t_+^0}{F} I_{\text{app}}, -D_{i,\text{eff}} \left.\frac{\partial c_2}{\partial x}\right\|_{x=L_{\text{sep}}} = -\frac{1-t_+^0}{F} I_{\text{app}}$
Modified Ohm's law (ionic phase)	$\mathbf{i}_2 = -\kappa_{\text{eff}} \nabla \Phi_2 + \frac{2\kappa_{\text{eff}} RT}{F}\left(1+\frac{\partial \ln f_\pm}{\partial \ln c_2}\right)\left(1-t_+^0\right)\nabla \ln c_2$	[11]	$i_2\|_{x=L_{\text{sep}}} = i_{0,\text{Li}}\left[\exp\left(-\frac{\alpha_a F}{RT}\Phi_2\right) - \exp\left(\frac{\alpha_c F}{RT}\Phi_2\right)\right]$
Current balance	$\nabla \cdot \mathbf{i}_2 = 0$	[12]	$i_2\|_{x=0} = I_{\text{app}}$
Li redox reaction (Butler-Volmer equation)	$I_{\text{app}} = i_{0,\text{Li}}\left[\exp\left(\frac{\alpha_a F}{RT}\left(\Phi_{\text{Li}}\right\|_{x=0} - \Phi_2\right)\right) - \exp\left(-\frac{\alpha_c F}{RT}\left(\Phi_{\text{Li}}\right\|_{x=0} - \Phi_2\right)\right)\right], i_{0,\text{Li}} = F k_{\text{Li}} c_2^{\alpha_a}$	[13]	

used in expressions for σ_{eff}, κ_{eff}, $D_{\text{i,eff}}$. While the volume fraction of the conducting phase is obtained from the cathode composition, tortuosity is not easily measured and is usually correlated with the volume fraction through the Bruggeman relation [20,21]

$$\tau = \gamma \varepsilon^{1-\alpha} \quad [15]$$

This is a generalized form of Bruggeman equation with constant coefficients γ and α that varies with electrode morphology and composition. In the present study, the volume fraction of the conductive phase is ca. 0.6; the Bruggeman coefficients are taken from literature[22] to obtain $\tau = 24$ ($\gamma = 18$, $\alpha = 1.5$).

We now use equations 3–15 to analyse our experimental data. Measurements of the potential as a function of current density obtained in a symmetric lithium-lithium cell with PS-PEO electrolyte are shown in Figure 3. The cell potential is a sum of the potential drop across the separator and the kinetic drop at the lithium metal/separator interfaces. The exchange current density at the lithium/PS-PEO interface was obtained by fitting the current-potential data[23] to equations 10–12 in Table I using the rate constant, k_{Li}, as the adjustable parameter and the transport properties described above. The comparison between theory and experiment is shown in Figure 3 and the exchange current density ($i_{0,\text{Li}}$) obtained is 5.5 A/m^2.

For the LiFePO$_4$/PS-PEO interface, the exchange current density was taken from literature,[14] neglecting effects due to differences in the electrolyte. A low rate discharge (10 μA/cm^2 or C/10) data is assumed to represent the dependency of the equilibrium potential (U_{eq}) on lithium concentration in the active particles.

This completes the parameter estimation needed for the simulations. Table II lists the parameters used in the model for the Li/LiFePO$_4$ cell and Li/Li symmetric cell.

Results and Discussion

In Figures 4a and 4b we show the experimentally obtained potential vs. capacity (symbols) during discharge of the Li/LiFePO$_4$ cell at different current densities ranging from 10 to 80 μA/cm^2. It is evident that the experimental discharge curves are a strong function of current density. The solid curves in Figure 4a show model predictions using the parameters in Table II. To a good approximation, the theoretical predictions are independent of current density. There is thus a qualitative disagreement between theory and experiments implying that the parameters used in the model do not reflect the real properties of the composite cathode; we expect the model to accurately describe the separator and the Li-metal anode. In traditional batteries, the decrease in the end-of-discharge electrode capacity is due to mass transport limitations, while the potential drop during the early stages of discharge is due to a combination of ohmic and kinetic losses and mass transport limitations in the battery. At least one of these limitations has not been accurately described in the model.

The electronic conductivity of the P3HT-PEO/LiTFSI mixture (open symbols in Figure 2a) was measured in the absence of LiFePO$_4$ particles. The addition of LiFePO$_4$ particles could lead to additional effects that are not captured by conductivity measurements in the absence of the particles: (i) The potential dependent oxidation of P3HT is affected by the presence of the redox active LiFePO$_4$. (ii) The

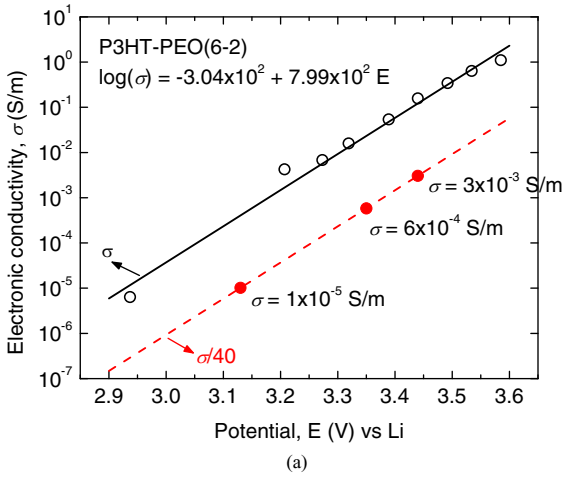

(a)

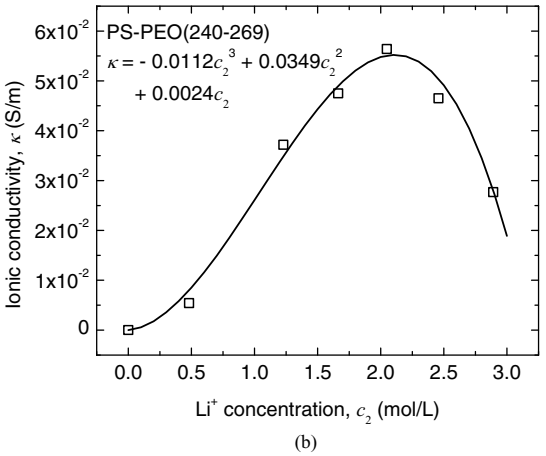

(b)

Figure 2. (a) Electronic conductivity of the oxidized P3HT-PEO block copolymer as a function of cell potential, and (b)ionic conductivity of PS-PEO block copolymer as a function of electrolyte concentration. Open symbols are experimental data; solid lines are the fits to the experimental data. These fits are used in the model calculations. The dashed line in Figure 2a is the linear fit divided by 40 (σ/40), and the three constant conductivities denoted by the closed symbols are used to calculate the discharge curves in Figure 8. The data is taken from Figure 9 of ref 4.

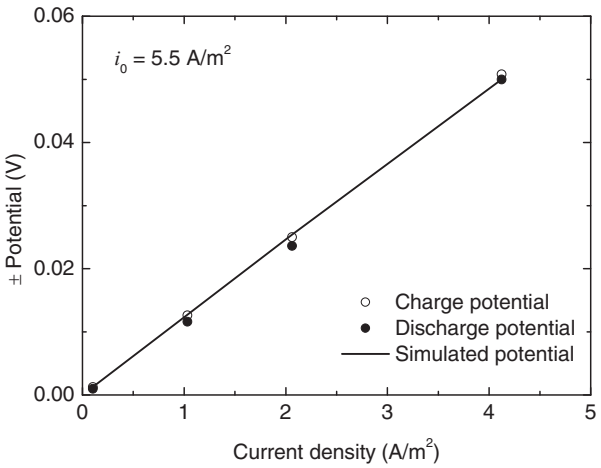

Figure 3. Experimental and calculated potentials for a Li/Li symmetric cell with a PS-PEO polymer electrolyte layer for different current densities. The exchange current density of the lithium stripping reaction (5.5 A/m^2) was obtained by fitting the model to the experimental data.

Schottky barrier that forms between the semiconducting polymer and the conducting carbon coating on the $LiFePO_4$. (iii) Additional contact resistance at the polymer/particle interface. These factors would increase the resistance to electron transport in the cathode. To capture this effect, we reduced the electronic conductivity (σ vs. E in Figure 2a) by a constant factor until agreement between theory and experiment was obtained. We found that replacing σ by σ/40 resulted in good agreement between the model and experiments. The dashed line in Figure 2a shows the conductivity used in the modified model calculations. The model predictions based on σ/40 are shown by solid curves in Figure 4b. Note that σ over a large potential window is higher than κ (Figures 2a and 2b). However, σ/40 is lower than κ regardless of potential. The data in Figures 2 and 4 suggest that the electronic transport in the cathode limits the performance of our battery. While the simulation results at 40 and 80 μA/cm^2 do not fit the data perfectly, the predictions are remarkable considering the uncertainty in the numerous parameters necessary to perform the calculations. The parameter we have focused on, σ, has been adjusted by a constant factor (i.e., σ/40 instead of σ). This factor could very well depend on the SOC and potential. This may be one of many reasons for the

Table II. List of electrode and transport parameters used in the models for Li/$LiFePO_4$ cell and Li/Li symmetric cell.

Parameter	Value	Reference
Thickness		
Cathode	5 μm	Measured
Electrolyte	43 μm (Li/$LiFePO_4$ cell)	Measured
	36 μm (Li/Li symmetric cell)	Measured
Particle radius (r_p)	52 nm	Estimated
Volume fraction		
$LiFePO_4$	0.414	Measured
P3HT-PEO (ε)	0.586	Measured
Conductivity		
Electronic (σ)	Figure 2a	4
Ionic (κ)	Figure 2b	Measured
Ionic of $LiPF_6$ in EC/DEC	Figure 2–9 in Ref 25	25
Diffusion coefficient		
Lithium in $LiFePO_4$ (D_{Li})	8×10^{-18} m^2/s	14
Lithium ion in P3HT-PEO and PS-PEO (D_i)	7.8×10^{-12} m^2/s	19
Lithium ion in PC/EC/DMC	Equation (14) in Ref 26	26
Exchange current density (referenced at 2 M and 50% SOC)		
$LiFePO_4$ (i_0)	0.3 A/m^2	14
Lithium metal ($i_{0,Li}$)	5.5 A/m^2	Fitted to experimental data
Transference number (t_+^0)	0.41	27

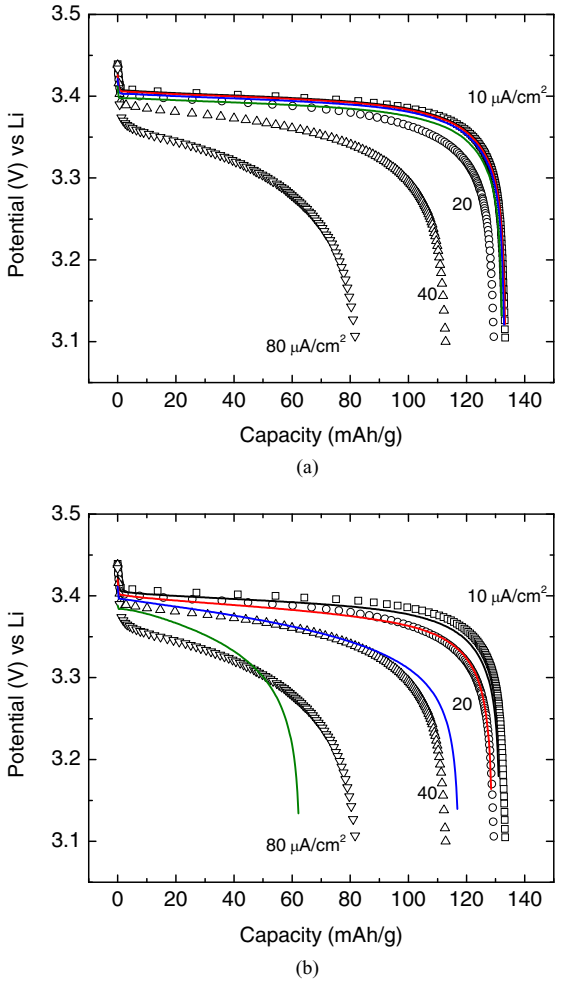

Figure 4. Model-experiment comparison of discharge potential *versus* capacity for the $LiFePO_4$/P3HT-PEO electrode at various rates. The model predictions were obtained by using the parameters listed in Table II (4a), and a reduced electronic conductivity of σ/40 (4b). Symbols are experimental values and lines are model fits. An applied current of 10 μA/cm^2 corresponds to C/10.

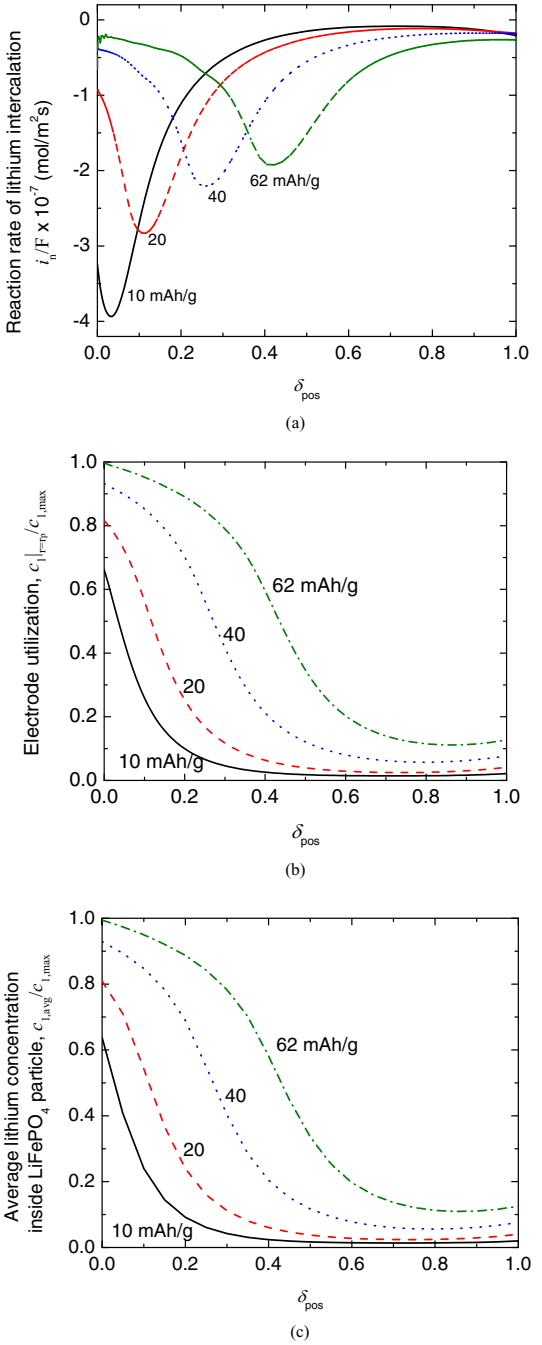

Figure 5. Reaction rate of lithium intercalation (a), electrode utilization (b), and average lithium concentration (c) across the cathode during different stages of discharge using an electronic conductivity of σ/40. The applied current is 80 μA/cm^2. The abscissa of 0 represents the current collector, and 1 represents the separator. At the end of discharge (62 mAh/g), the reaction front is at $\delta_{pos} = 0.4$ (5a) and more than half of the electrode ($\delta_{pos} > 0.4$) is below 50% of utilization (5b and 5c). Note the similarity between figures 5b and 5c, suggesting that solid phase transport is not limiting.

departures between simulations and experiments seen at high rates in Figure 4b.

We now examine the consequence of the electronic conductivity limitations of our system and the implications of the varying electronic conductivity with potential. In Figure 5a, we plot the rate of lithium intercalation reaction vs. the dimensionless distance from the current collector ($\delta_{pos} = x/L_{pos}$, $0 < x < L_{pos}$) at a discharge current density of 80 μA/cm^2. At the beginning of discharge (10 mAh/g), the reaction takes place preferentially near the current collector; the rate of reaction is largest at approximately $\delta_{pos} = 0.03$. This occurs because the electronic conductivity of P3HT is lower than the ionic conductivity of PEO. As discharge proceeds, the active particles are lithiated and the reaction front moves toward the separator. At the end of discharge (62 mAh/g), the largest rate of reaction occurs at $\delta_{pos} = 0.4$, meaning that the rest of the electrode ($0.4 < \delta_{pos} < 1$) is not completely lithiated before the cell hits the cut-off potential. In contrast, in conventional batteries, the reaction rate at the beginning of discharge is largest in the vicinity of the $\delta_{pos} = 1.0$ and the reaction front moves toward the current collector as discharge proceeds.

In Figure 5b, we plot the electrode utilization vs. δ_{pos} at a discharge current density of 80 μA/cm^2. The utilization is defined as the ratio of lithium concentration at the surface of the active material particles to the maximum lithium concentration that can be inserted into the particles ($c_1|_{r=r_p}/c_{1,max}$). At the early state of discharge (10 mAh/g), the utilization decreases rapidly with increasing δ_{pos} from a value of 0.66 at $\delta_{pos} = 0$ to negligibly small values at $\delta_{pos} = 0.4$ and beyond. As discharge proceeds, the utilization at $\delta_{pos} = 0$ increases and increasing utilization is observed at other values of δ_{pos}. At a capacity of 62 mAh/g, electrode utilization at $\delta_{pos} = 0$ is unity and this, by definition, is the end of discharge. At this stage, approximately half the electrode particles are not lithiated. In contrast, in conventional batteries based on liquid electrolyte where ionic conductivity dominates, the end of discharge occurs when the electrode utilization at $\delta_{pos} = 1$ is unity.

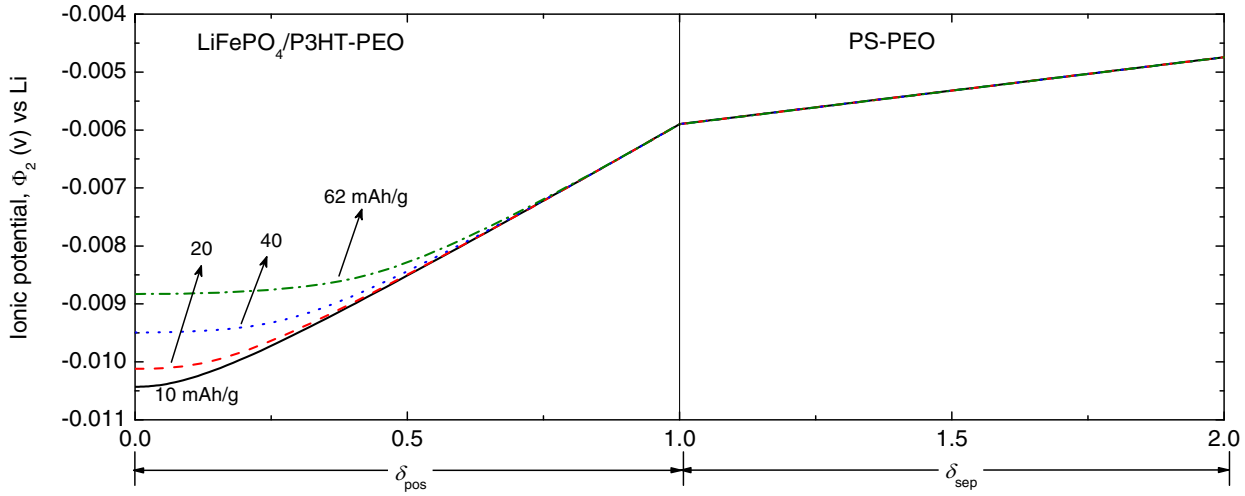

Figure 6. Ionic potential across the cell during discharge at 80 μA/cm^2. The abscissa of 0 represents the current collector; 1 represents the cathode/separator interface; 2 represents the separator/anode interface.

We also show the average lithium concentration inside the active material particles ($c_{1,avg}/c_{1,max}$) in Figure 5c. The concentration profiles in Figures 5b and 5c are almost identical, indicating that the concentration gradients within the active particles are unimportant. In other words, uncertainty related to the lithiation mechanism and D_{Li} do not affect our calculations.

In Figure 6, we plot the ionic potential vs. δ_{pos} and δ_{sep} ($1+(x-L_{pos})/L_{sep}$, $L_{pos} < x < L_{sep}$) at a discharge current density of 80 μA/cm^2. The potential is calculated referenced to the lithium anode. The potential drop at anode (ca. 4.7 mV) is due to the kinetic resistance of the lithium oxidation reaction. The potential drop across the separator is mainly due to ohmic effects and independent of the depth of discharge. The ionic potential drop in the cathode decreases with increasing depth of discharge because ions travel through a shorter distance as discharge proceeds and therefore lead to a decrease in ohmic drop. The magnitude of ionic potential drops (4 to 6 mV at 80 μA/cm^2) across the cathode and the separator is negligible compared to the overall potential drop (ca. 3.3 V) observed in Figure 4.

In Figure 7, we plot the electronic conductivity (σ/40) vs. δ_{pos} at a discharge current density of 80 μA/cm^2. The dependency of electronic potential, Φ_1, on δ_{pos} is captured by the right hand ordinate of Figure 7. As discharge proceeds, the lithiation near the current collector (Figure 5) leads to a decrease in the local electronic potential, which in turn leads to a decrease in conductivity. This decrease is relatively shallow at low depths of discharge (10 mAh/g). However, at the end of discharge (62 mAh/g) the electronic conductivity near the current collector is as low as 1×10^{-5} S/m because the electronic potential decreases to 3.1 V. The low electronic conductivity holds back the reaction from further propagating into the electrode as the electronic current must travel through a resistive path to reach the active particles that are away from the current collector. It is convenient to define $\Delta\Phi_1 = \Phi_1(\delta_{pos} = 1) - \Phi_1(\delta_{pos} = 0)$, which is the electronic potential drop across the entire cathode. $\Delta\Phi_1$ increases dramatically as discharge proceeds from a value of about 0.02 V at 10 mAh/g to 0.26 V at 62 mAh/g.

The importance of the dependency of electronic conductivity on cathode potential is shown in Figure 8, which compares the discharge potentials calculated using the potential-dependent electronic conductivity (σ/40) to calculations using constant electronic conductivities. Three constant values were selected: (i) 3×10^{-3} S/m, which corresponds to the initial conductivity at the beginning of discharge (0 mAh/g); (ii) 6×10^{-4} S/m, which corresponds to the conductivity at the middle of discharge (30 mAh/g); (iii) 1×10^{-5} S/m, which corresponds to the conductivity at the end of discharge (62 mAh/g). Also shown in Figure 8 are experimental potential vs. capacity data at a current density of 80 μA/cm^2. The experimental data shows a continuous change in slope as discharge proceeds. In contrast, the predicted

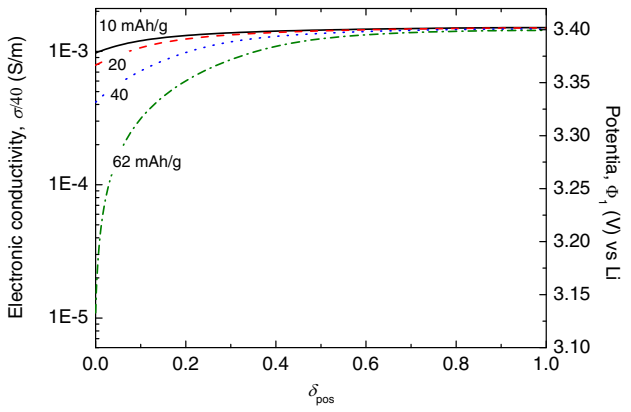

Figure 7. Electronic conductivity (σ/40) (left ordinate) and potential (right ordinate) across the cathode electrode at different states of discharge at the discharge rate of 80 μA/cm^2.

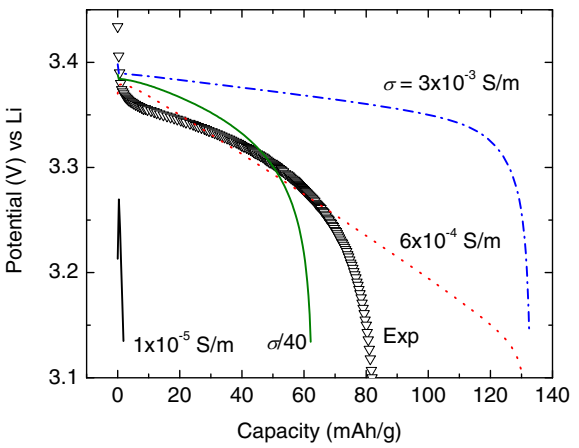

Figure 8. Calculated electrode potential versus capacity using different values of constant electronic conductivity (corresponding to the closed symbols in Figure 2a). Also shown are the experimental data and calculation based on a potential-dependent conductivity (σ /40).

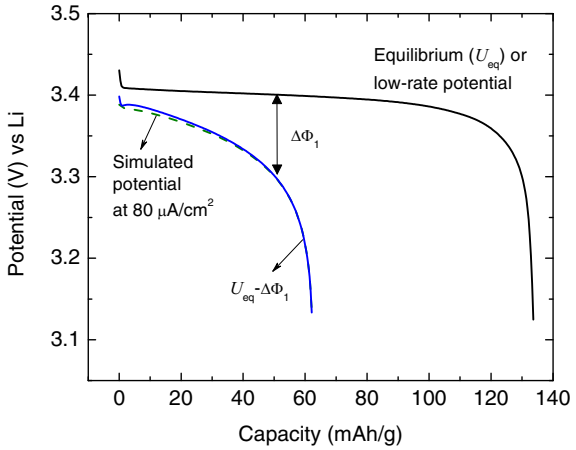

Figure 9. Calculated potential drops in the cell at a current density of 80 μA/cm^2. $\Delta\Phi_1$ is the potential drop across the electronically conductive matrix in cathode from the current collector to the separator.

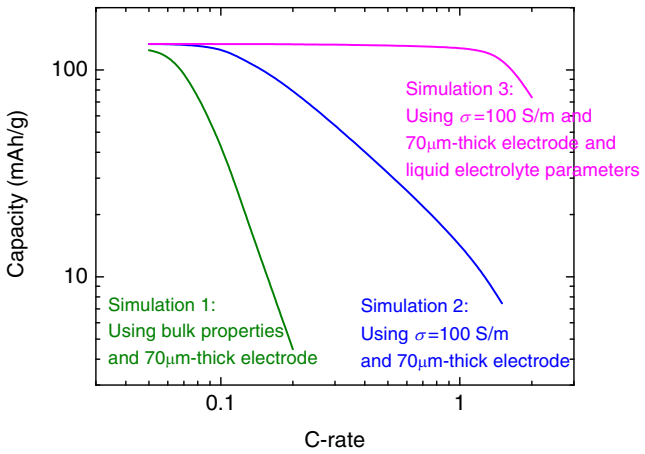

Figure 10. Modified Peukert plot showing the effect of electronic and ionic conductivities and lithium diffusion coefficient on the end-of-discharge capacity of a 70 μm-thick electrode. The difference between Simulation 1 and Simulation 2 is due to the electronic resistance in the conductive matrix. The difference between Simulation 2 and Simulation 3 is due to the ionic resistance in the solid block copolymer. The liquid electrolyte parameters, ionic conductivity and diffusion coefficient, are taken from reference 25 and 26, and listed in Table II.

discharge curves for the three constant electronic conductivities show slopes that are independent of time as discharge proceeds until the very end of discharge. Predictions based on the largest conductivity (3×10^{-3} S/m) show a small ohmic drop and the electrode retains most of its capacity (135 mAh/g), unlike the experiment where discharge capacity is 80 mAh/g. Predictions based on the intermediate conductivity (6×10^{-4} S/m) are consistent with the potential data at the early stages of discharge but deviations are evident toward the later stages of discharge. Importantly, predictions indicate full capacity retention at the end of discharge (135 mAh/g), which is significantly higher than the experimental value (80 mAh/g). Predictions based on the lowest conductivity (1×10^{-5} S/m) are completely inconsistent with the experimental data. It should be clear from Figure 8 that accounting for the dependency of electronic conductivity on potential is essential for qualitatively and quantitatively predicting the discharge curves.

The model can also be used to assess the potential drops that limit the electrode performance. When appreciable current flows through the electrode, a number of resistances can drive the electrode away from equilibrium, including ohmic resistances due to electronic and ionic current flow, kinetic resistances due to charge-transfer reactions, and transport resistances due to salt and lithium diffusion. We address this issue in Figure 9 where we show an equilibrium potential curve (U_{eq} as a function of capacity) calculated at an extremely low rate (1 μA/cm^2 or C/100) where all limitations are negligible. Also shown in Figure 9 is the dependency of U_{eq}-$\Delta\Phi_1$ on capacity and the simulated discharge curve with all the resistances (dashed line, same as in previous figures) at a current of 80 μA/cm^2. The two curves are essentially indistinguishable indicating that the majority of the potential drop occurs in the cathode due to low electronic conductivity.

The simulation results suggest that charging at a fixed rate would result in better utilization of the cathode due to the increase in conductivity with potential. We hope to address this point in future studies. It is important however to know that even in conventional electrodes with PVDF/carbon black-based composites in a liquid electrolytes, $LiFePO_4$ cathodes can be charged much faster than they can be discharged.[24] While the phenomenon is not well understood, analysis of charging studies at different rates with the semiconducting polymer will need to account for this effect.

In the discussion above we have focused on the characterization of an all-solid lithium battery wherein electronic and ionic transport occurs through polymers. Both electronic and ionic transport rates in these batteries are much lower than those in conventional lithium batteries based on liquid electrolytes. It is therefore not surprising that we have to use relatively thin cathode (ca. 5 μm) in this study. It is important to use simulations to guide the development of the next-generation of polymeric materials that may enable practical batteries with thicker electrodes. We attempt to do this in Figure 10 where we show capacity vs. C-rate curves (modified Peukert plot) for three different model calculations. The first simulation (Simulation 1) uses the bulk properties of the conducting polymer binder and electrolyte, including the electronic (σ, not σ/40) and ionic conductivities and diffusion coefficient for a cathode thickness of 70 μm. This simulation would represent the best-case scenario for the present polymer system. It is evident that even in this case, the capacity drops significantly as rate increases, and at a discharge rate of C/5, the capacity at the end of discharge is only 5 mAh/g. In Figure 10 we also show simulation results obtained when the polymer electronic conductivity is fixed at 100 S/m, independent of potential (Simulation 2). One expects this behavior if the polymer electronic conductivity was no longer the bottleneck. It is evident from this simulation that at a rate of C/5 the capacity is significantly higher (80 mAh/g) than that in Simulation1. Discharge capacities are negligible above 1 C. We contrast these simulations on polymeric materials with a simulation using 1 M $LiPF_6$ in ethylene carbonate/diethyl carbonate (1:1 by weight) as the liquid electrolyte (Simulation 3) and $\sigma = 100$ S/m. It is evident that the decrease in capacity between C/10 and 1 C is due to the poor ionic transport properties in polymeric systems.

Conclusions

In this paper we study the discharge characteristics of a battery consisting of a cathode with $LiFePO_4$ particles in a P3HT-PEO copolymer matrix that conveys electrons and ions to the active particles, a PS-PEO copolymer electrolyte layer, and a lithium metal anode by experiments and simulations. The electronic conductivity of P3HT is potential-dependent. The main advance in this work is to quantify the effect of this potential dependency on battery performance. Simulations show that the electronic conductivity of the polymer in the cathode is a factor of 40 lower than that obtained from measurements in the absence of active particles. Further work is required to understand the reason for this observation. In the future, we will try to measure the effective electronic conductivity of composite cathodes comprising $LiFePO_4$ particles in a P3HT-PEO copolymer as a function of potential. These measurements are non-trivial and require the introduction of a nickel mesh in the interior of the cathode.[4] Unlike conventional batteries wherein reaction fronts move from the electrode/separator interface to the current collector, reaction fronts in the present system move from the current collector toward the electrode/separator interface.

The potential-dependent conductivity is manifested in the shape of the discharge curve wherein the slope increases continuously with capacity. This effect cannot be captured when predictions are made using a potential-independent electronic conductivity wherein a rapid change in slope is only seen at the very end of discharge. The simulations are used to provide targets for the development of practical batteries with polymers that simultaneously conduct both electrons and ions.

Acknowledgments

This work was supported as part of the Joint Center for Energy Storage Research, an Energy Innovation Hub funded by the U.S. Department of Energy (DOE), Office of Science, Basic Energy Sciences (BES).

List of Symbols

a	specific surface area of active material, 1/m
c_1	lithium concentration in the active material, mol/m^3
$c_{1,avg}$	average lithium concentration inside active material particles, mol/m^3
$c_{1,max}$	maximum lithium concentration that can be inserted into active material particles, mol/m^3
c_2	salt concentration, mol/m^3 of electrolyte
D_i	ionic diffusion coefficient, m^2/s
D_{Li}	diffusion coefficient of lithium in the active material, m^2/s
F	Faraday's constant, 96,487 C/mol
$f_\pm$	mean molar activity coefficient of electrolyte
I_{app}	applied current in the cell, A/m^2
i_0	exchange current density of lithium insertion reaction at the surface of active material, A/m^2
$i_{0,Li}$	exchange current density of lithium redox reaction at lithium anode, A/m^2
i_1	superficial current density in the electronic-conductive phase, A/m^2
i_2	superficial current density in the ionic-conductive phase, A/m^2
i_n	reaction current normal to the surface of active material, A/m^2
k	rate constant of lithium insertion reaction at surface of active material, (A/m^2)/(C/mol)/(mol/m^3)$^{1.5}$
k_{Li}	rate constant of lithium redox reaction at lithium anode, (A/m^2)/(C/mol)/(mol/m^3)$^{0.5}$
L	thickness, m
R	universal gas constant, 8.314 J/mol/K
r	radial position across a spherical particle, m
r_0	molar ratio of lithium ions to ethylene oxide moieties
r_p	radius of active material particle, m
T	temperature, K
t	time, s
t_+^0	transference number of lithium ion with respect to solvent velocity
U_{eq}	equilibrium potential, V
x	distance from current collector/cathode interface, m

Greek

α_a	anodic transfer coefficient, 0.5
α_c	cathodic transfer coefficient, 0.5
δ	dimensionless distance from current collector/cathode interface
ε	volume fraction of block copolymer in the cathode
κ	ionic conductivity, S/m
σ	electronic conductivity, S/m
Φ	electrical potential, V
Φ_{Li}	electrical potential of lithium metal, V

Subscripts

pos	positive electrode
eff	effective value
sep	separator
1	electronic-conductive phase
2	ionic-conductive phase

References

1. J.F. Mike and J.L. Lutkenhaus, *Journal of Polymer Science Part B: Polymer Physics*, **51** (2013) 468.
2. A.E. Javier, S.N. Patel, D.T. Hallinan, V. Srinivasan, and N.P. Balsara, *Angewandte Chemie International Edition*, **50** (2011) 9848.
3. S.N. Patel, A.E. Javier, G.M. Stone, S.A. Mullin, and N.P. Balsara, *ACS Nano*, **6** (2012) 1589.
4. S.N. Patel, A.E. Javier, and N.P. Balsara, *ACS Nano*, **7** (2013) 6056.
5. M. Singh, O. Odusanya, G.M. Wilmes, H.B. Eitouni, E.D. Gomez, A.J. Patel, V.L. Chen, M.J. Park, P. Fragouli, H. Iatrou, N. Hadjichristidis, D. Cookson, and N.P. Balsara, *Macromolecules*, **40** (2007) 4578.
6. A. Panday, S. Mullin, E.D. Gomez, N. Wanakule, V.L. Chen, A. Hexemer, J. Pople, and N.P. Balsara, *Macromolecules*, **42** (2009) 4632.
7. J.S. Newman and C.W. Tobias, *Journal of The Electrochemical Society*, **109** (1962) 1183.
8. M. Doyle, T.F. Fuller, and J. Newman, *Journal of The Electrochemical Society*, **140** (1993) 1526.
9. J. Newman and W. Tiedemann, *AIChE Journal*, **21** (1975) 25.
10. T.F. Fuller, M. Doyle, and J. Newman, *Journal of The Electrochemical Society*, **141** (1994) 1.
11. A.K. Padhi, K.S. Nanjundaswamy, and J.B. Goodenough, *Journal of The Electrochemical Society*, **144** (1997) 1188.
12. A. Yamada, Y. Kudo, and K.-Y. Liu, *Journal of The Electrochemical Society*, **148** (2001) A1153.
13. C. Delacourt, P. Poizot, J.-M. Tarascon, and C. Masquelier, *Nature Materials*, **4** (2005) 254.
14. V. Srinivasan and J. Newman, *Journal of The Electrochemical Society*, **151** (2004) A1517.
15. L. Laffont, C. Delacourt, P. Gibot, M.Y. Wu, P. Kooyman, C. Masquelier, and J.M. Tarascon, *Chemistry of Materials*, **18** (2006) 5520.
16. C.V. Ramana, A. Mauger, F. Gendron, C.M. Julien, and K. Zaghib, *Journal of Power Sources* **187** (2009) 555.
17. C. Delmas, M. Maccario, L. Croguennec, F.L. Cras, and F. Weill, *Nature Materials*, **7** (2008) 665.
18. G. Brunetti, D. Robert, P. Bayle-Guillemaud, J.L. Rouvière, E.F. Rauch, J.F. Martin, J.F. Colin, F. Bertin, and C. Cayron, *Chemistry of Materials*, **23** (2011) 4515.
19. S.A. Mullin, G.M. Stone, A. Panday, and N.P. Balsara, *Journal of The Electrochemical Society*, **158** (2011) A619.
20. V.D.A.G. Bruggeman, *Annalen der Physik*, **24** (1935) 636.
21. I.V. Thorat, D.E. Stephenson, N.A. Zacharias, K. Zaghib, J.N. Harb, and D.R. Wheeler, *Journal of Power Sources*, **188** (2009) 592.
22. D.E. Stephenson, E.M. Hartman, J.N. Harb, and D.R. Wheeler, *Journal of The Electrochemical Society*, **154** (2007) A1146.
23. D.T. Hallinan, S.A. Mullin, G.M. Stone, and N.P. Balsara, *Journal of The Electrochemical Society*, **160** (2013) A464.
24. V. Srinivasan and J. Newman, *Electrochemical and Solid-State Letters*, **9** (2006) A110.
25. S.G. Stewart, Ph.D. dissertation, *Determination of Transport Properties and Optimization of Lithium-ion Batteries* (2007).
26. L.O. Valøen and J.N. Reimers, *Journal of The Electrochemical Society*, **152** (2005) A882.
27. D.T. Hallinan and N.P. Balsara, *Annual Review of Materials Research*, **43** (2013) 503.